JACS Au
AN OPEN ACCESS JOURNAL OF THE AMERICAN CHEMICAL SOCIETY

pubs.acs.org/jacsau
Article

Protein-Driven Electron-Transfer Process in a Fatty Acid Photodecarboxylase

Giacomo Londi,* Giacomo Salvadori, Patrizia Mazzeo, Lorenzo Cupellini, and Benedetta Mennucci*

Cite This: JACS Au 2025, 5, 158−168
Read Online

ABSTRACT: Naturally occurring photoenzymes are rare in nature, but among them, fatty acid photodecarboxylases derived from *Chlorella variabilis* (*Cv*FAPs) have emerged as promising photobiocatalysts capable of performing the redox-neutral, light-induced decarboxylation of free fatty acids (FAs) into C1-shortened *n*-alka(e)nes. Using a hybrid QM/MM approach combined with a polarizable embedding scheme, we identify the structural changes of the active site and determine the energetic landscape of the forward electron transfer (fET) from the FA substrate to the excited flavin adenine dinucleotide. We obtain a charge-transfer diradical structure where a water molecule rearranges spontaneously to form a H-bond interaction with the excited flavin, while the FA's carboxylate group twists and migrates away from it. Together, these structural modifications provide the driving force necessary for the fET to proceed in a downhill direction. Moreover, by examining the R451K mutant where the FA substrate is farther from the flavin core, we show that the marked reduction of the electronic coupling is counterbalanced by an increased driving force, resulting in a fET lifetime similar to the WT, thereby suggesting a resilience of the process to this mutation. Finally, through QM/MM molecular dynamic simulations, we reveal that, following fET, the decarboxylation of the FA radical occurs within tens of picoseconds, overcoming an energy barrier of ∼0.1 eV. Overall, by providing an atomistic characterization of the photoactivation of *Cv*FAP, this work can be used for future protein engineering.

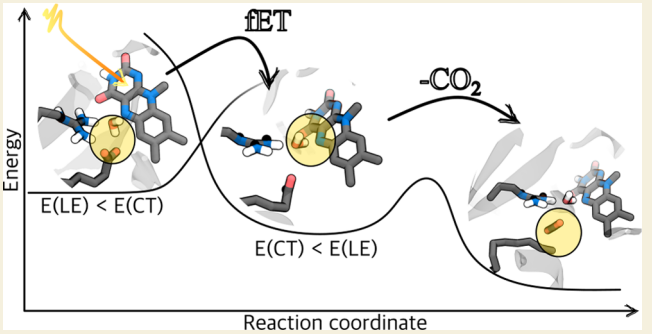

KEYWORDS: *photoenzymes, photobiocatalysis, fatty acid photodecarboxylase, QM/MM, electron transfer, decarboxylation*

INTRODUCTION

The synergy between bio- and photocatalysis offers numerous benefits and intriguing challenges,[1−3] and photobiocatalysis using enzymes has gained significant interest over the past few decades. This interest is driven by a dual objective: to extract new functions from known enzymes and to develop new enzymes that facilitate essential biological reactions.[4−11] Unlike enzymes with latent photochemical activity that can be engineered for photocatalytic reactions,[12] in natural photoenzymes, a prosthetic cofactor within the enzyme's active site becomes excited upon light absorption and promotes electron or energy transfer to convert an organic substrate into a given product.[13−15]

Among the very few examples of known natural photoenzymes, the fatty acid photodecarboxylase (FAP; see Figure 1a),[16,17] discovered in the microalgae *Chlorella variabilis* (*Cv*FAP) NC64A, stands out for its ability to perform redox-neutral, light-induced decarboxylation of free fatty acids (FAs) into C_1-shortened *n*-alka(e)nes. This process, triggered by the photoexcitation of a flavin adenine dinucleotide (FAD) cofactor noncovalently bound to the protein, has promising applications in the production of chemicals, pharmaceuticals, cosmetics, and, most importantly, biofuels.[18−21] Though *Cv*FAP shows a marked preference for mid- to long-chain FAs (*i.e.*, the highest activity was observed for the C_{16}−C_{17} chain length), over the years, researchers have shown that wild-type (WT) FAPs can be used to synthesize biofuels from triglycerides,[22] long-chain aliphatic amines and esters from FAs,[23] and many other hydrocarbons.[24−26] Moreover, considerable efforts have been made to expand the substrate scope via reaction condition engineering to operate on short and medium carboxylic acids,[27] via enzyme engineering, thereby expressing FAP mutants to improve the catalytic activity toward medium- to long-chain FAs,[28] or to produce biogas, such as propane and butane.[29] Recently, Yang and co-workers have demonstrated that FAPs can be repurposed to catalyze novel stereoselective radical reactions in naturally occurring photoenzymes.[30] By employing rational enzyme engineering and directed evolution on *Cv*FAP, they developed

Received: September 16, 2024
Revised: November 29, 2024
Accepted: December 4, 2024
Published: December 18, 2024

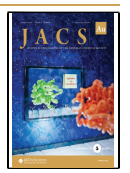

https://doi.org/10.1021/jacsau.4c00853
JACS Au 2025, 5, 158−168

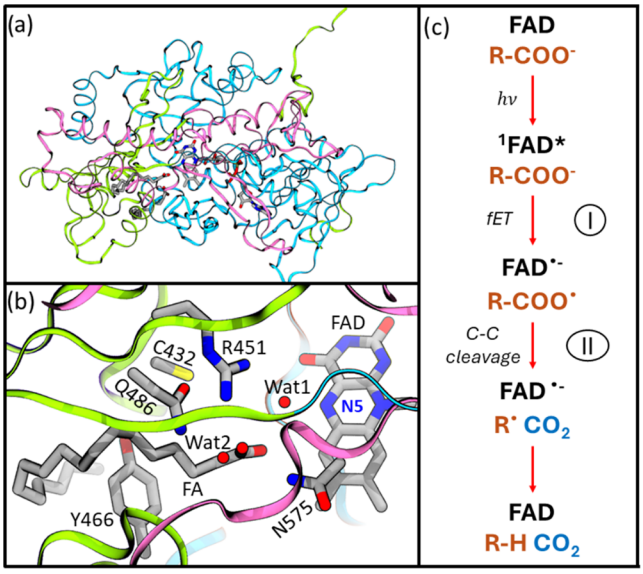

Figure 1. (a) Wild-type *Cv*FAP (RSCB PDB entry: 6YRU), where the FAD cofactor and the two stearic acids are shown, while protein loops are represented with different colors: the N-terminal domain (light blue) is responsible for the binding and stabilization of the FAD cofactor; the C-terminal domain (magenta) for the substrate/product trafficking; in yellow, the interdomain residues; (b) a zoom on the enzyme's active site as found in the crystal structure in the dark at 100 K; and (c) the catalytic steps studied in this work: (I) the forward electron transfer (fET) and (II) the decarboxylation process as a result of a C−C bond cleavage.

a series of stereoselective radical photocyclases, thereby suppressing the *n*-alka(e)ne R−H product and leading to radical C−C bond formation. These studies clearly indicate that a comprehensive understanding of the mechanism of *Cv*FAP's photoactivation, as well as the characterization of the role of the environment in this process, is highly valuable for establishing clear principles to guide the design of optimized functionalities through mutations.

In their seminal study, Sorigué et al. provided a detailed characterization of the FAP's catalytic cycle by combining crystallographic and spectroscopic techniques, supported by computational studies.[17] As in Figure 1b showing the enzyme's active site as found in the crystal structure of the WT *Cv*FAP, the carboxylate group of a stearic acid in its deprotonated form (R-COO$^-$, where R = $C_{17}H_{35}$) is stabilized near the FAD cofactor by H-bonding interactions with two water molecules, Wat1 and Wat2, and the side chains of two neighboring residues, R451 and N575. Upon blue-light irradiation, the FAD chromophore is excited to a singlet excited-state ^{1}FAD* that oxidizes the carboxylate group of the FA. The resulting forward electron transfer (fET) is very efficient with a quantum yield (QY) > 80%, leading to the formation of the anionic semiquinonic FAD$^{\bullet-}$ and the R-COO$^\bullet$ radical species. By means of ultrafast transient fluorescence and absorption spectroscopy, the authors confirmed what was previously found by performing temporal lower-resolution measurements:[16] the ^{1}FAD* is quenched in ∼300 ps, and the formation of FAD$^{\bullet-}$ is concomitant with ^{1}FAD* decay. Quantum-chemical calculations proposed that upon photoexcitation Wat1 close to the flavin rearranges and forms a H-bond with N5 of FAD, thus driving the electron transfer. Moreover, by using time-resolved infrared spectroscopy, it was observed that CO_2 begins to develop in the active site with the same time scale as the ^{1}FAD* quenching, meaning that the decarboxylation process is rate-limited by the fET. At last, the CO_2 dissociation was found to be barrierless.

Starting from these findings, in this work, we provide an atomistic characterization of the protein-driven structural and energetic features of the photoactivation of *Cv*FAP. To reach this goal, we integrate hybrid quantum mechanics/molecular mechanics (QM/MM) strategies,[31−34] within static and dynamic descriptions of the fET process and the subsequent decarboxylation process, as depicted in Figure 1c. From our QM/MM simulations, we determine that the fET process involves a charge-transfer (CT) state where Wat1 rearranges and forms a H-bond interaction with the N5 of the excited flavin. Such a rearrangement of Wat1 is a direct consequence of a H-bond disruption between Wat1 and the twisted carboxylate group of the FA substrate. Yet, the fET takes place *before* Wat1 has completed its rearrangement. In the WT *Cv*FAP, this occurs when the electronic interaction between the FA and excited flavin is still significant. We also find that the rearrangement of Wat1 stabilizes the CT state energy and, together with the FA's structural repositioning, provides the required driving force for the fET to occur in a downhill fashion. To deepen the characterization of the fET process in *Cv*FAP, we also investigate the impact of an R451K mutation, where the presence of a protonated lysine (instead of an arginine) and more water molecules in the active site (with respect to the WT) contributes to keeping the FA substrate

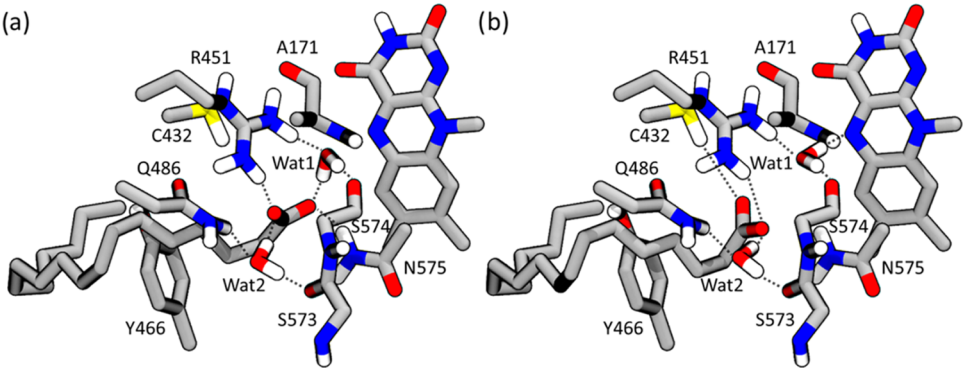

Figure 2. (a) The structure of the wild-type *Cv*FAP active site optimized (a) at the ground state [FAD R-COO$^-$] and (b) at the CT diradical state [FAD$^{\bullet-}$R-COO$^\bullet$]. Black-dashed lines represent the H-bond network formed by the fatty acid's carboxylate group and the two water molecules, Wat1 and Wat2.

https://doi.org/10.1021/jacsau.4c00853
JACS Au 2025, 5, 158−168

farther from the excited flavin. We find that the reduced electronic interaction between the two molecular partners is counterbalanced by a much larger driving force, making the fET possible with a lifetime comparable to the WT. Thus, the reduced catalytic activity measured in the R451K mutant should be sought in other steps of the cycle, as our data suggest a resilience of the fET process to this specific mutation. Finally, by investigating the decarboxylation in the WT *Cv*FAP with both static and dynamic QM/MM approaches, we show that the process involves an energy barrier of ∼0.1 eV that is overcome in tens of picoseconds, in agreement with a recent computational study.[35]

RESULTS AND DISCUSSION

Structural Rearrangements upon FAD Excitation

Figure 2a displays the WT *Cv*FAP active site in the [FAD R-COO$^-$] optimized structure as obtained by using a QM/MM model based on density functional theory (DFT) (see the Methods section for details). By choosing as the QM region the C_9−COO$^-$ fragment of the FA, the flavin isoalloxazine core, the protonated R451 residue, Wat1 and Wat2, we found that, with respect to the crystal structure (Figure S1), the most substantial rearrangements involve the distances between the two water molecules and their H-bond partners, namely the carbonyl backbone of S573 and S574 and the side-chain amide of Q486 (Table S1). We also note that the so-called "butterfly bend angle" of flavin is increased by ∼6° compared to what was found in the crystal structure (23.2° vs 17.4°), which influences the vertical electron affinity (see the discussion in the Supporting Information and Table S2). Additionally, the FA's dihedral angle O1−C1−C2−C3 planarizes reaching 8°, thereby forming a much stronger H-bond interaction with the side-chain amide of N575. This complex H-bond network formed by the FA's carboxylate group with neighboring residues and water molecules is meant to avoid an over-stabilization due to the presence of the protonated R451 and an inactivating bidentate interaction. We anticipate that upon fET the flow of the negative charge toward the flavin core reduces the electrostatic interaction between the FA's carboxylate group and the protonated R451, leading to a subsequent rearrangement of the FA's structure.

To have a consistent description of the locally excited (LE) state on the flavin core and the CT state, as well as their relative energy ordering at the different optimized scenarios, we used the Tamm−Dancoff approximation (TDA) formulation of time-dependent (TD) DFT. This choice was suggested by previous computational works on photoinduced electron transfers in light-harvesting complexes and flavin-based photoreceptors.[36,37] TDA DFT QM/MM optimization of the [^{1}FAD* R-COO$^-$] structure (see the Methods section), where the flavin is photoexcited to a $\pi \rightarrow \pi^*$ LE state, results in little change from the ground-state [FAD R-COO$^-$] optimized scenario. On the other hand, major rearrangements take place in the CT diradical system [FAD$^{\bullet-}$ R-COO$^\bullet$] generated after the fET from the FA to the excited flavin in its LE state. As shown in Figure 2b (Table S1), the most striking structural rearrangements for the optimized CT state are (i) the formation of a H-bond between N5 of FAD and Wat1; (ii) the twist of the FA's dihedral angle O1−C1−C2−C3 from 6 to 62°. In particular, the hydrogen bond distance between Wat1 and N5 of FAD changes from 2.97 Å at the ground state [FAD R-COO$^-$] to 1.79 Å at the CT state [FAD$^{\bullet-}$ R-COO$^\bullet$], while that one between the Wat1 and O1 of FA changes from 1.77 to 4.18 Å. As a result of the fET and a reduced electronic density on the carboxylate group, the electrostatic interaction between the neutral, radical FA and the protonated R451 is mitigated. In such a conformation, the twisted carboxylate group is also less stabilized by H-bond interactions with waters and neighboring residues: it keeps the H-bond interactions (though weaker) with Wat2 and the side-chain amide of R451 and forms a new, weak one with the side-chain thiol of C432, thereby hinting at a possible role of the C432 residue in the stabilization of the CT diradical system [FAD$^{\bullet-}$ R-COO$^\bullet$].

In Figure 2b, it is interesting to observe how, by means of our QM/MM optimization of the CT diradical state, Wat1 spontaneously rearranges at the excited state and forms a new H-bond with N5 of FAD, in response to a H-bond disruption between the carboxylate group and Wat1 itself. These structural changes have profound implications for the enzyme's catalytic function that will be discussed in the next section. Yet, we anticipate that the progressive spacing between the FA's carboxylate group and the excited flavin will have a dramatic effect on their electronic coupling.

Forward Electron-Transfer Mechanism and Timescale

We turn our discussion to the analysis of the excited-state potential energy surfaces (PES) of the LE and CT states. At each of the optimized structures, we performed a polarizable embedding QM/MM energy calculation (see the Methods section). Additionally, by exploiting a geodesic interpolation algorithm,[38] we generated intermediate structures, thereby building a reaction pathway connecting the three optimized structures (see the Supporting Movie).

As can be seen in Figure 3, the lowest-lying LE state (red solid line) is at 3.27 eV at the Franck−Condon structure of [FAD R-COO$^-$], while the CT state (solid blue line) is significantly higher at 4.40 eV. We note that, between these two states, there are two more LE states at 3.75 eV (a mixed $\pi \rightarrow \pi^*$/n $\rightarrow \pi^*$ state) and at 3.81 eV (a $\pi \rightarrow \pi^*$ state) in agreement with a recent benchmark study on flavin's low-lying excited states.[39] The electronic coupling V_{ET} (gray stars in Figure 3) between the LE and CT states at the Franck−Condon structure amounts to 18 meV. As the system evolves toward the optimized LE state minimum [^{1}FAD* R-COO$^-$] (the vertical dashed line in Figure 3), the energy of the LE state decreases to 2.99 eV, and V_{ET} with the higher-lying CT state slightly increases to 23 meV. Again, above the low-lying LE state, two additional LE states lie at 3.68 and 3.79 eV, but due to these higher energies, we do not expect them to participate in the fET process. At its minimum geometry, the CT state [FAD$^{\bullet-}$ R-COO$^\bullet$] becomes the lowest excited state at 2.69 eV. Here, V_{ET} has dramatically collapsed to 0.1 meV, as the FA's carboxylate group rolls away from the flavin core. In Figures S2 and S4, we report the natural transition orbitals, which clearly show the characters of the different excited states for the three optimized scenarios.

With the data at hand (Table S3), we calculated the fET rate for the process [^{1}FAD* R-COO$^-$] (2) → [FAD$^{\bullet-}$ R-COO$^\bullet$] (3) by using the semiclassical Marcus theory,[40,41] which reads as follows

$$\kappa_{fET} = \frac{2\pi}{\hbar}\|V_{ET}\|^2 \sqrt{\frac{1}{4\pi\lambda k_B T}} \exp\left[\frac{-(\Delta E + \lambda)^2}{4\lambda k_B T}\right]$$

where $\hbar$ is the reduced Planck's constant, k_B is the Boltzmann constant, T is the temperature, λ is the reorganization energy

https://doi.org/10.1021/jacsau.4c00853
JACS Au 2025, 5, 158−168

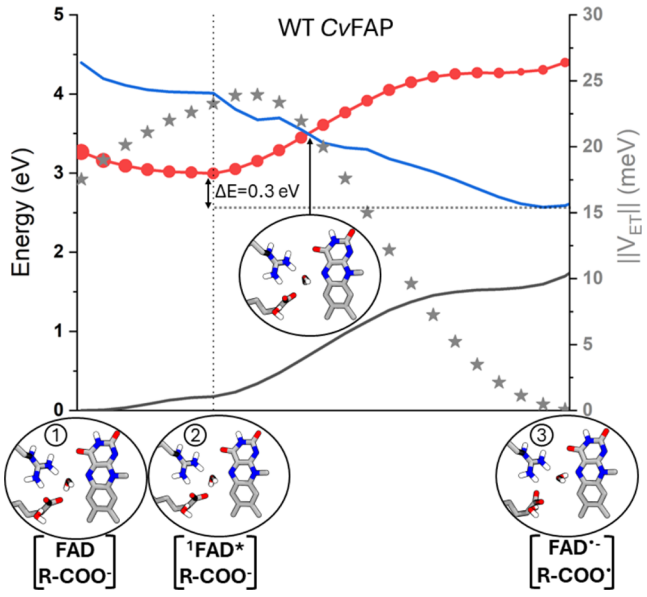

Figure 3. Potential energy surfaces of the ground state (in black), the lowest-lying locally excited (LE, in red), and charge transfer (CT, in blue) along the reaction pathway. The normalized oscillator strength of the LE state is represented by the size of the full red circles along its PES. The round panels show the coordinates of the QM atoms according to different scenarios: (1) [FAD R-COO$^-$], (2) [^{1}FAD* R-COO$^-$], (3) [FAD$^{\bullet-}$ R-COO$^\bullet$], and at the LE-CT crossing point. Data are listed in Table S3. The LE-CT energy difference at their minima is also reported along with the absolute value (in meV) of the electronic couplings V_{ET} (gray stars) in the right *y*-axis.

computed as the average between the forward and backward relaxation energies, and ΔE is the LE-CT energy difference. Despite its approximations, the Marcus theory has been successfully applied to describe electron-transfer processes in numerous biological systems.[37,42−44] Here, its application is particularly well-justified, as the electronic couplings are significantly smaller than the reorganization energies ($V_{ET} \ll \lambda$). Moreover, it is interesting to note that, within the framework of the Marcus theory, in our case, the ET occurs at the crossing between the LE and CT PES, where V_{ET} is still high (Figure 3) and the FA's carboxylate group is close to the flavin core at 3.5 Å. By monitoring the IP and EA evolution along the reaction pathway (Figure S5), it can indeed be observed that immediately after the LE-CT crossing, the IP of the deprotonated FA becomes smaller than the IP of the flavin: it becomes thus easier to remove an electron from the HOMO of the deprotonated FA than that of the flavin. The parameters feeding the Marcus theory's equation to describe the fET were computed at the polarizable embedding QM/MM level obtaining λ = 1.44 eV, ΔE = −0.30 eV, and V_{ET} = 20 meV at the LE-CT crossing. From these data, we obtained a rate of $\kappa_{fET} = 8.4 \times 10^8$ s^{-1}, which translates into a timescale for the fET of 1.2 ns, in reasonable agreement with the experimental observation of ∼300 ps, though 4 times larger.

To investigate the origin of such an overestimation, we checked the numerical robustness of the calculated parameters by recalculating them with a different exchange−correlation functional. The two DFT functionals here tested (namely ωB97X-D and CAM-B3LYP) have been largely used to characterize electron/charge-transfer processes involving flavin derivatives.[39,45,46] We initially examined the magnitude of the electronic coupling V_{ET}, but we observed no significant difference. In fact, at the LE-CT PES crossing, we calculated V_{ET} = 18 meV compared to 20 meV (Table S3 and Figure S6), concluding that the magnitude of V_{ET} does not depend on the QM/MM level of theory. Even the reorganization energy λ was found to be consistent between the two chosen functionals: λ = 1.49 *eV* compared to 1.44 eV. Here, we note that our model is expected to underestimate the λ value because the contribution of the nuclear reorganization of the outer sphere is missing as the environment was kept frozen during the QM/MM optimizations. Conversely, the fast electronic response of the environment to the LE → CT transition is correctly captured by our polarizable embedding QM/MM calculations (see the Methods section). Regarding the ΔE parameter, the calculated LE-CT energy difference is now significantly larger (ΔE = −0.57 eV compared to −0.30 eV), as a result of a different stabilization of the CT state described by the two functionals. Such a change in ΔE finally leads to a rate of $\kappa_{fET} = 1.8 \times 10^{10}$ s^{-1} and a timescale of 55 ps, which now is 5 times faster than the experimental data. The sensitivity of the ΔE parameter to the chosen DFT functional is clearly a critical aspect of the simulation as the exponential dependence of the Marcus rate to ΔE makes it highly dependent on even small variations of ΔE. This indicates that our simulations are better suited for estimating the timescale's order of magnitude rather than its precise absolute value. However, our calculations clearly show that the experimental measured timescale is possible only if the CT state is significantly stabilized with respect to the LE state. This contrasts with previous simulations,[17] where the two states were found to be almost isoenergetic.

We conclude this section by pointing out the role of Wat1 in the fET process. Upon examination of the structure observed at the LE-CT crossing (top round panel in Figure 3), it is notable that, although the carboxylate group of FA has initiated its twisting motion, with a dihedral angle of O1−C1−C2−C3 of 24°, Wat1 has not fully completed its rearrangement. This indicates that, even though the rearrangement of Wat1 occurs at the excited state, it does not necessarily facilitate the fET. Truly, the rearrangement of Wat1, and consequently the formation of a new H-bond between N5 of FAD and Wat1, strongly stabilizes the CT state at the expense of the LE state (Figure S7 and Table S4), but it is not intrinsically sufficient to promote an efficient fET. In fact, our results demonstrate that both the rearrangement of Wat1 and the associated FA's structural shifts (*i.e.*, the rotation of the carboxylate group and its overall departure from the flavin core) occur as a direct consequence of the fET process. These protein-driven structural changes within the enzyme's active site provide the necessary driving force for the fET to occur in a downhill fashion. Moreover, the protonated R451 residue forms strong H-bonds with the FA's carboxylate group, stabilizing the substrate in a configuration close to the flavin core, thus yielding a sizable coupling (V_{ET} = 20 meV) at the LE-CT PES crossing. This arrangement is crucial as it ensures that the fET is fast enough to outcompete other detrimental processes such as intersystem crossing (ISC) to ^{3}FAD*. In contrast, the V_{ET} = 0.1 meV calculated in the CT minimum, where Wat1 is fully rearranged and the carboxylate group is 4.5 Å from the flavin core, would slow the fET to several hundreds of nanoseconds. Under these conditions, ISC would prevail, leading to a decay to the ground state [FAD R-COO$^-$].

https://doi.org/10.1021/jacsau.4c00853
JACS Au 2025, 5, 158−168

Impact of the R451K Mutation on the Electron-Transfer Process

We further investigate the impact of the R451K mutation on the fET in *Cv*FAP. This mutation, where a protonated arginine is replaced by a protonated lysine, was originally introduced to understand the role of R451 in the catalytic cycle, ascribed to be the final proton donor to the alkyl radical $R^{\bullet}$.[17] Replacing arginine with lysine (*e.g.*, a stronger proton donor) resulted in a faster fluorescence decay of ^{1}FAD* than in the WT without substrate (*i.e.*, in the absence of the fET). Two main hypotheses were made to explain this finding: (i) the fET in the R451K mutant takes place with the same timescale (hundreds of picoseconds) as in the WT but there is an inverse amplitude ratio between the fast fET (∼15%) and the slower ISC to ^{3}FAD* (∼85%); (ii) the fET in the R451K mutant occurs more slowly than in WT (in tens of nanoseconds) and with a higher QY than in (i) (30−40%) but still smaller than in the WT. It was also proposed that the marked reduction in fET QY might be due to an increased distance between FA and ^{1}FAD*, combined with an overstabilization of the carboxylate group by an additional water molecule Wat3, which replaces the amine group of the R451 originally present in the WT.

To investigate such mutant with our QM/MM model, we chose as the QM region the FA C_9−COO^-, the flavin core, the protonated K451, Wat1, Wat2, and Wat3. As a result of the optimization of the three scenarios [FAD R-COO^-], [^{1}FAD* R-COO^-], and [$FAD^{\bullet-}$ R-$COO^{\bullet}$] (Figure S9, Table S5, and Supporting Movie), the distance between the FA's carboxylate group and the flavin core remains overall constant at ∼4 Å and in any case larger than in the WT. In addition, the hydrogen bond distance between Wat1 and N5 of FAD changes from 3.16 Å at the ground state [FAD R-COO^-] to 2.05 Å at the CT state [$FAD^{\bullet-}$ R-$COO^{\bullet}$] (vs from 2.97 to 1.79 Å in the WT), while that one between Wat1 and O1 of FA from 1.90 to 2.69 Å (vs from 1.77 to 4.18 Å in the WT), with the FA's dihedral angle O1−C1−C2−C3 going from 76 to 59° (vs from 6 to 62° in the WT). On the one hand, these structural differences with respect to the WT significantly affect the magnitude of V_{ET}, which is now approximately 4−5 times smaller than in the WT. On the other hand, the excitation energy of the LE state at its minimum increases of ∼0.1 eV, while that of the CT state slightly decreases with respect to the WT: the LE state at the optimized [^{1}FAD* R-COO^-] structure lies at 3.12 eV, while the CT state at the optimized [$FAD^{\bullet-}$ R-$COO^{\bullet}$] structure lies at 2.65 eV (Figure 4). The LE and CT natural transition orbitals are shown in Figures S10−S12 for the three optimized scenarios.

Overall, with λ = 1.25 eV, V_{ET} = 4 meV at the LE-CT crossing, and ΔE = −0.47 eV, the calculated fET rate for the R451K mutant is $\kappa_{fET} = 2.0 \times 10^9$ s^{-1}, corresponding to a timescale (∼500 ps) of the same order of magnitude as the one calculated for the WT *Cv*FAP. These findings clearly support the experimental hypothesis (i), which implies an unchanged fET rate but with an inverted amplitude ratio of the fast and slow phases.

Finally, it is important to highlight that in the R451K mutant, the FA's carboxylate group is not stabilized by H-bond interactions with K451, but with nearby water molecules. As a result, a close and strong interaction with the flavin core (Figure S9) is no longer possible. Yet, our calculations show that fET can take place with a similar timescale of the WT. This can be explained by considering that the reduced V_{ET} is

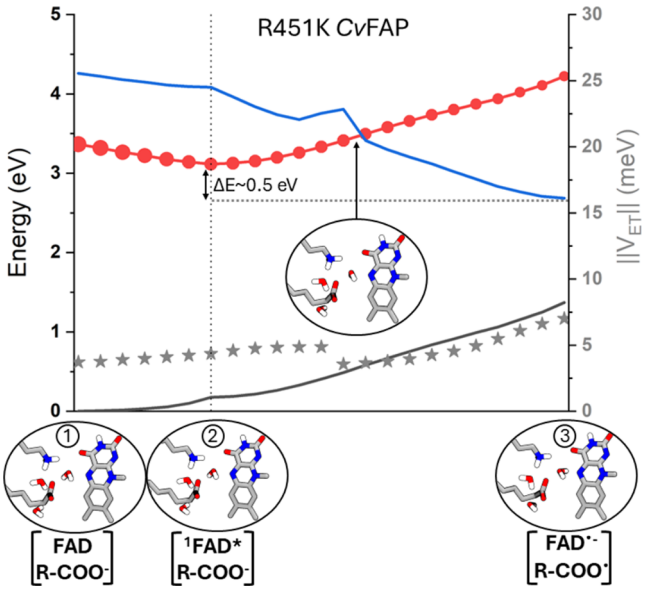

Figure 4. Potential energy surfaces of the R451K mutant ground state (in black), lowest-lying locally excited (LE, in red), and charge transfer (CT, in blue) along the reaction pathway. The normalized oscillator strength of the LE state is represented by the size of the full red circles along its PES. The round panels show the coordinates of the QM atoms according to the scenario: (1) [FAD R-COO^-], (2) [^{1}FAD* R-COO^-], and (3) [$FAD^{\bullet-}$ R-$COO^{\bullet}$], and at the LE-CT crossing point. Data are listed in Table S6. The LE-CT energy difference at their minima is also reported, along with the absolute value (in meV) of the electronic couplings V_{ET} (gray stars) in the right *y*-axis.

now counterbalanced by a larger ΔE (in absolute value), suggesting an interesting interplay between the two main parameters that govern the Marcus equation. Moreover, also in the R451K mutant, the rearrangement of Wat1, although contributing to the stabilization of the CT state (Figure S13 and Table S7), *alone* is not sufficient to ensure a rapid fET. Once again, it is the fET that drives the structural rearrangements within the active site's architecture, thereby ensuring that the fET occurs in a downhill fashion.

In summary, our data suggest that in the R451K mutant, the fET takes place with a similar timescale of the WT, potentially hinting at a resilience of the process to this specific mutation. Therefore, according to our results, the observed reduced activity of the R451K mutant must be ascribed to other steps in the catalytic cycle. We finally note that a different mutation of the same residue, *i.e.*, an alanine replacing the protonated arginine,[17] makes *Cv*FAP completely inactive, due to the absence of a positively charged residue near the FA substrate, which is not anymore deprotonated, and thus cannot be photoreduced by the excited flavin. This can be explained by the fact that a fast fET is made possible only if the CT state can be stabilized with respect to the LE by a proper electrostatic environment, where the role of the nearby protonated residue is of utmost importance.

Decarboxylation Mechanism

We address now decarboxylation through the FA's C−C bond cleavage, for which we first calculated the energetic barrier of the process by performing a relaxed scan along the bond length C1−C2 of the radical C_9−$COO^{\bullet}$. In this model, only the FA radical is treated at the QM level in an unrestricted DFT formalism, whereas the flavin is treated classically but by using

https://doi.org/10.1021/jacsau.4c00853
JACS Au 2025, 5, 158−168

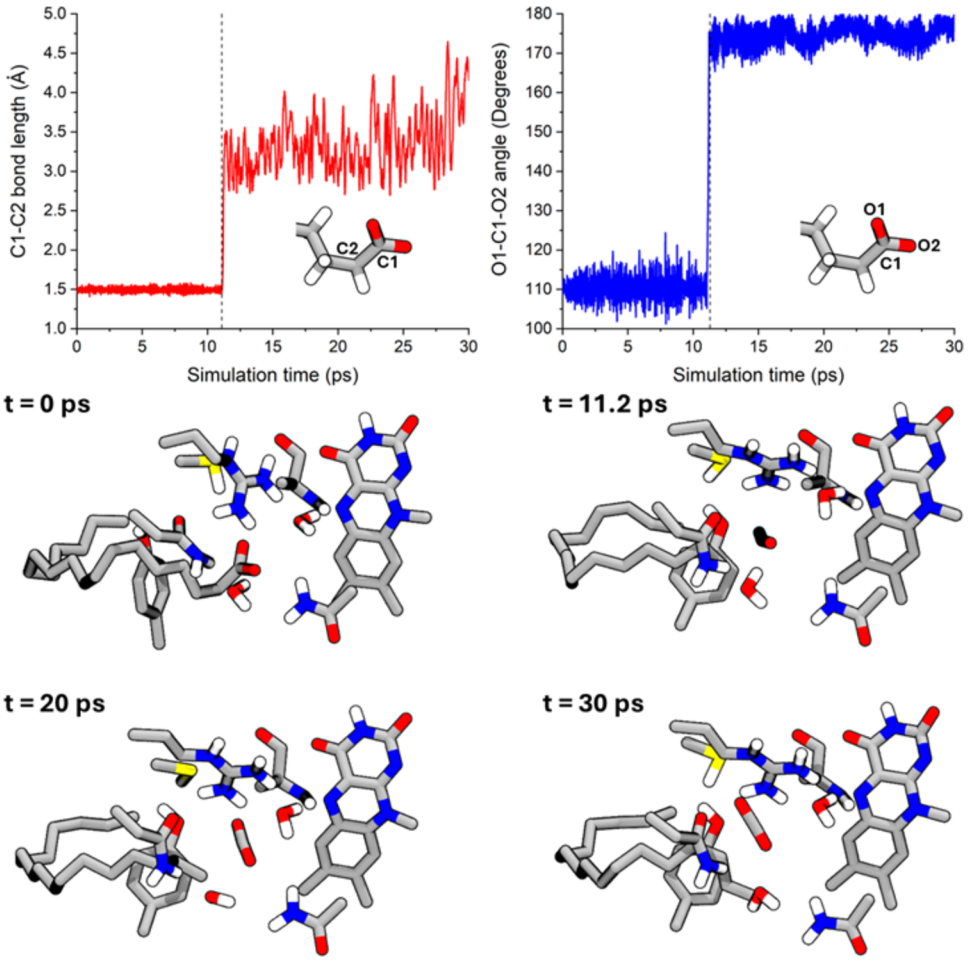

Figure 5. Fatty acid's bond length C1−C2 (in red) and bending angle O1−C1−O2 (in blue) as a function of the QM/AMOEBA MD simulation time, along with four snapshots extracted at different times. Figure S18 shows the steep change in the two degrees of freedom upon decarboxylation at time t = 11.2 ps, while other snapshots at different times are reported in Figure S19.

MM atomic charges to electrostatically mimic the anionic semiquinone $FAD^{\bullet -}$ species. To validate our findings, we compared the obtained structures with a model in which both the FA radical and $FAD^{\bullet -}$ species were included in the QM region. To properly describe such diradical species, we employed the ΔSCF DFT method.[47,48] The two models yielded very similar structures (Figure S14). Based on this evidence, from now on, we shall discuss only the results obtained with the simpler model.

The potential energy profile steeply increases by 0.20 eV when starting from a C1−C2 equilibrium distance of 1.49 Å for the reactant and arriving at 1.63 Å (Figure S15). Afterward, the radical decarboxylates, and the product $[C_9^{\bullet} + CO_2]$ is 0.25 eV more stable than the reactant (with a C1···C2 distance of 2.89 Å). The authors of ref 17 chose the bending angle O1−C1−O2 as the reaction coordinate, obtaining a barrierless process: this is confirmed by our calculations when we repeated the relaxed scan along the same coordinate (Figure S16). To refine our estimation of the barrier, we optimized the transition state, thereby identifying a single normal mode with an imaginary frequency that drives decarboxylation (Figure S17). Considering free-energy corrections for the QM part, the product is now more stable than the reactant by 0.38 eV and the energy barrier for decarboxylation is 0.11 eV: this activation energy, according to transition-state theory, corresponds to a rate of 9.1×10^{10} s^{-1} and a timescale of 11 ps. Our results align with a previous study on carbonyloxy radical compounds,[35] where decarboxylation was computed to occur in tens of picoseconds after the fET and, in any case, an order of magnitude faster than the ET process.

In light of this evidence, we tried to obtain the same process in real time by performing a 30 ps QM/AMOEBA molecular dynamics (MD) simulation, where the radical $C_9-COO^{\bullet}$ is treated at the unrestricted DFT level (see the Methods section for details). We indeed observed the decarboxylation taking place at approximately 11 ps (Figure 5), in agreement with our estimation of the barrier height. A spin density analysis on the radical FA performed before and after the decarboxylation is shown in Figure S20, while structural properties as a function of the QM/AMOEBA MD simulation time are shown in Figures S21−S30.

Experimentally, after the decarboxylation, the $FAD^{\bullet -}$ species undergoes oxidization within ∼100 ns, resulting in a transiently red-shifted FAD_{RS} species, while the primary alkyl radical $R^{\bullet}$ is converted into the alkane product R−H. Clearly, our QM/AMOEBA MD simulation is too short to allow any strong conclusion regarding this step of the catalytic cycle and cannot describe the process as it would require the inclusion of FAD and other nearby residues in the QM part (for instance, the protonated R451 as the proton donor, as proposed by ref 17). However, throughout the trajectory (see the Supporting Movie), the flavin butterfly angle C4−N5−N10−C9 assumes

https://doi.org/10.1021/jacsau.4c00853
JACS Au 2025, 5, 158−168

even larger values than those observed in the crystal structure (~40° vs 17.4°; Figure S21), although time-resolved serial fs crystallography measurements suggest that the flavin core does not undergo significant light-induced conformational changes[17] within our simulation time, we observe that the closest hydrogen atom to $R^{\bullet}$ is the one of Wat2 (around 3 Å; Figure S24), while R451 is further (around 4 Å; Figure S25). Additionally, N5 of FAD appears to form a stronger H-bond with the closer Wat1 at the expense of the backbone of A171 (Figures S29 and S30).

It remains to be determined whether these structural features are retained once back ET from $FAD^{\bullet-}$ takes place and which is the species that accepts back the electron (presumably the alkyl radical $R^{\bullet}$, as proposed by ref 17). This information would be important to unveil the origin and nature of the FAD_{RS} species and to reveal whether the back ET triggers some further structural changes within the enzyme's active site. Finally, we remark that, so far, two independent studies proposed distinct termination mechanisms of the catalytic cycle for which the R−H product is formed and the oxidized FAD cofactor is restored: one involving a hydrogen atom transfer from a nearby cysteine C432 residue[49] and another suggesting a proton-coupled (back) electron-transfer mechanism with the participation of a water molecule and a protonated arginine R451 as a proton donor.[17] The latter is, nowadays, the most credited proposed mechanism, although a definitive explanation of the real mechanism is still missing. Such a challenging task will be properly addressed in a follow-up work, with the aim of exploring the enzyme's active site complex architecture and to finally unravel the mechanism underlying the subsequent steps of the catalytic cycle.

CONCLUSIONS

By means of hybrid QM/MM approaches coupled with a polarizable model for the protein, we explored the structural features and energetic landscape of the photoinduced ET of *Cv*FAP. We obtained that the measured experimental timescale of ~300 ps is possible only due to a large stabilization of the CT state thanks to the rearrangement of the enzyme's active site, where a water molecule (Wat1) plays a paramount role by forming a H-bond interaction with the excited flavin. However, for fET to occur, this rearrangement of Wat1 must be coupled to a structural adjustment of the FA substrate, involving a twisted carboxylate group and a shift away from the flavin core. Together, these structural modifications within the active site provide the driving force necessary for the fET to proceed in a downhill direction.

To deepen this analysis, we examined the same process in the R451K mutant, where the interaction between the protonated lysine and the FA is absent, causing the substrate to be positioned farther from the flavin core. Our calculations indicate that the resulting decrease in the electronic coupling is counterbalanced by an increased LE-CT energy gap, thus maintaining the calculated fET lifetime comparable to that of the WT. This suggests that the fET process exhibits resilience to this mutation. Together, the results on the WT and R451K mutant provide valuable insights into the protein-driven fET mechanism, which crucially depends on structural rearrangements within the active site, on the electronic interaction between the FA and flavin core, and on the LE-CT energy difference.

Finally, we characterized the decarboxylation process in the WT *Cv*FAP by finding a very small energetic barrier, which is overcome in 11 ps. The same timescale was confirmed by performing a polarizable QM/MM MD simulation and observing in real time the FA's C−C bond cleavage and the CO_2 development. All of these findings confirm that the decarboxylation process occurs in a much shorter timescale than the fET itself as recently found by Aleksandrov et al.[35] and contrary to what was suggested in a previous study by Zhong and co-workers on the dynamics evolution of *Cv*FAP with femtosecond spectroscopy.[50]

METHODS

The crystallographic structure (RSCB PDB entry: 6YRU, solved at 100 K in the dark at a 1.78 Å resolution)[17] was used as the starting point for our simulations on the wild-type (WT) *Cv*FAP. Missing residues at the end of the C-terminal loop were modeled using Modeller 10.5.[51] Protonation states were assigned with MCCE (multiconformation continuum electrostatics)[52,53] software at pH 8.5, optimal for the photoenzyme's activity in solution, and histidine protonation states were further checked by visual inspection. As a result, the protein is electrically neutral. The total charge of the system is −4 due to two deprotonated FAs and the $[FAD]^{2-}$ cofactor. No counterions were added to neutralize the system. Missing hydrogen atoms were introduced with the *leap* tool available in Amber22.[54] The same procedure was repeated for the R451K mutant (RSCB PDB entry: 6YS1 solved at 100 K in the dark at a 1.64 Å resolution),[17] with the only exception that, as a result of the MCCE calculation, the protein at pH = 8.5 has charge −1 and therefore the total charge of the system is −5.

All of the residues were described with the ff14SB force field,[55] water molecules with the TIP3P model,[56] and the FAs with the general Amber force field (gaff).[57] The parameters for the FAD cofactor were obtained by taking the literature flavin mononucleotide (FMN) parameters[58] and completing them with the ones of the adenosine diphosphate (ADP).[59] Restrained electrostatic potential (RESP) charges for the FA and the FMN cofactor were calculated at the MP2/*aug*-cc-pVDZ level of theory in a water medium mimicked by a polarizable continuum model (PCM).[60] The crystal structure was finally subjected to molecular mechanics (MM) energy minimization (2000 conjugate gradient steps) with Amber22 to relax only the crystallographic water molecules and all of the hydrogen atoms of the protein, substrates, and cofactor. Heavy atoms (except water oxygens) were restrained by applying a 100 kcal mol^{-1} $Å^{-2}$ harmonic potential.

A density functional theory (DFT) optimization was performed on the system by means of the ONIOM (electrostatic embedding) QM/MM scheme,[61] as implemented in the Gaussian16 suite of programs.[62] Except where otherwise stated, the QM region consists of the isoalloxazine flavin core, a shorter FA fragment (C_9−COO^-), the side chain of the protonated R451 (or K451 for the mutant), and two water molecules Wat1 and Wat2 (or three water molecules Wat1, Wat2, and Wat3 for the mutant), saturating open valences with link atoms. On top of the optimized [FAD R-COO^-] structure, Tamm−Dancoff approximation-based[63] DFT (TDA DFT) QM/MM optimizations were carried out to characterize two excited-state minima: [^{1}FAD* R-COO^-], where the flavin core is photoexcited in a locally excited (LE) $\pi \rightarrow \pi^*$ state, and [$FAD^{\bullet-}$ R-$COO^{\bullet}$], where the fET from the carboxylate group of the fatty acid to the excited flavin has occurred, giving rise to a charge-transfer (CT) diradical state. In performing such calculations, the QM system was described with the ωB97X-D exchange−correlation DFT functional and the 6-31+G-(d,p) basis set, while the MM region was kept frozen.

To account for the mutual polarization between the excited-state QM density and the environment in a polarizable embedding fashion, we resorted to polarizable embedding QM/MM calculations,[64,65] where the atomic multipole optimized energetics for biomolecular simulation (AMOEBA) force field was coupled to the QM methods.[66] The force field parameterization of the FMN, ADP, and FA was carried out following the protocol explained in a previous work.[67] On each optimized structure, single-point energy calculations were

https://doi.org/10.1021/jacsau.4c00853
JACS Au 2025, 5, 158−168

performed with the same level of theory as above by using the corrected linear response TDA DFT QM/AMOEBA scheme and additionally applying a state-specific polarization correction to the excitation energies. The electronic coupling for the photoinduced ET between the FA's carboxylate group and the excited flavin core was computed within the multistate fragment charge/excitation difference framework.[68−70] Besides the ωB97X-D functional, we also employed the CAM-B3LYP functional, where explicitly stated.

A QM/AMOEBA molecular dynamics (MD) simulation was run on the WT-optimized [$FAD^{\bullet-}$ R-$COO^{\bullet}$] structure upon solvation with water molecule added at 6 Å from the system. After minimization, a 30 ps long simulation was propagated in the NVT ensemble using the Bussi thermostat at room temperature,[71] with a time constant of 0.1 ps and an integration step of 0.5 fs, as previously done in other works.[48,72,73] Here, only the FA radical fragment C_9−$COO^{\bullet}$ was treated at the QM ωB97X-D/6-31G(d) level of theory, while the environment was described by the polarizable AMOEBA force field. To run such calculations, we used the machinery developed in our group by interfacing Tinker,[74] working as an MD engine and computing the bonded and van der Waals terms of the energy and forces, with a locally modified version of the Gaussian suite of programs,[75] which computes the QM/AMOEBA energy, forces, and electrostatic and polarization contributions.

■ ASSOCIATED CONTENT

Supporting Information

The Supporting Information is available free of charge at https://pubs.acs.org/doi/10.1021/jacsau.4c00853.

The wild-type *Cv*FAP structure and excited-state properties; the R451K mutant structure and excited-state properties; and decarboxylation mechanism in the wild-type *Cv*FAP (PDF)

Geodesic scan of the WT *Cv*FAP (AVI)

Geodesic scan of the R451K mutant (AVI)

30 ps QM/AMOEBA MD of the WT *Cv*FAP (AVI)

■ AUTHOR INFORMATION

Corresponding Authors

Giacomo Londi − *Department of Chemistry and Industrial Chemistry, University of Pisa, 56124 Pisa, Italy;* orcid.org/0000-0001-7777-9161; Email: giacomo.londi@dcci.unipi.it

Benedetta Mennucci − *Department of Chemistry and Industrial Chemistry, University of Pisa, 56124 Pisa, Italy;* orcid.org/0000-0002-4394-0129; Email: benedetta.mennucci@unipi.it

Authors

Giacomo Salvadori − *Institute for Computational Biomedicine (INM-9), Forschungszentrum Jülich, 52428 Jülich, Germany;* orcid.org/0000-0001-7330-6228

Patrizia Mazzeo − *Department of Chemistry and Industrial Chemistry, University of Pisa, 56124 Pisa, Italy;* orcid.org/0000-0002-7015-8124

Lorenzo Cupellini − *Department of Chemistry and Industrial Chemistry, University of Pisa, 56124 Pisa, Italy;* orcid.org/0000-0003-0848-2908

Complete contact information is available at: https://pubs.acs.org/10.1021/jacsau.4c00853

Author Contributions

CRediT: **Giacomo Londi** conceptualization, data curation, formal analysis, investigation, methodology, visualization, writing - original draft, writing - review & editing; **Giacomo Salvadori** data curation, formal analysis, methodology, visualization, writing - original draft, writing - review & editing; **Patrizia Mazzeo** formal analysis, methodology, visualization, writing - original draft, writing - review & editing; **Lorenzo Cupellini** conceptualization, methodology, software, supervision, writing - original draft, writing - review & editing; **Benedetta Mennucci** conceptualization, funding acquisition, methodology, resources, supervision, writing - original draft, writing - review & editing.

Notes

The authors declare no competing financial interest.

■ ACKNOWLEDGMENTS

G.L. and B.M. acknowledge funding by the European Research Council under the Grant ERC-AdG-786714 (LIFETimeS). L.C. and B.M. also thank the financial support from the University of Pisa (PRA_2022_34), ICSC-Centro Nazionale di Ricerca in High-Performance Computing, Big Data, and Quantum Computing, funded by the European Union-NextGenerationEU-PNRR, Missione 4 Componente 2 Investimento 1.4.

■ REFERENCES

(1) Litman, Z. C.; Wang, Y.; Zhao, H.; Hartwig, J. F. Cooperative Asymmetric Reactions Combining Photocatalysis and Enzymatic Catalysis. *Nature* **2018**, *560* (7718), 355−359.

(2) Schmermund, L.; Jurkaš, V.; Özgen, F. F.; Barone, G. D.; Büchsenschütz, H. C.; Winkler, C. K.; Schmidt, S.; Kourist, R.; Kroutil, W. Photo-Biocatalysis: Biotransformations in the Presence of Light. *ACS Catal.* **2019**, *9* (5), 4115−4144.

(3) Harrison, W.; Huang, X.; Zhao, H. Photobiocatalysis for Abiological Transformations. *Acc. Chem. Res.* **2022**, *55* (8), 1087−1096.

(4) Emmanuel, M. A.; Greenberg, N. R.; Oblinsky, D. G.; Hyster, T. K. Accessing Non-Natural Reactivity by Irradiating Nicotinamide-Dependent Enzymes with Light. *Nature* **2016**, *540* (7633), 414−417.

(5) Trimble, J. S.; Crawshaw, R.; Hardy, F. J.; Levy, C. W.; Brown, M. J. B.; Fuerst, D. E.; Heyes, D. J.; Obexer, R.; Green, A. P. A Designed Photoenzyme for Enantioselective [2 + 2] Cycloadditions. *Nature* **2022**, *611* (7937), 709−714.

(6) Sun, N.; Huang, J.; Qian, J.; Zhou, T.-P. P.; Guo, J.; Tang, L.; Zhang, W.; Deng, Y.; Zhao, W.; Wu, G.; Liao, R.-Z. Z.; Chen, X.; Zhong, F.; Wu, Y. Enantioselective [2 + 2]-Cycloadditions with Triplet Photoenzymes. *Nature* **2022**, *611* (7937), 715−720.

(7) Page, C. G.; Cooper, S. J.; Dehovitz, J. S.; Oblinsky, D. G.; Biegasiewicz, K. F.; Antropow, A. H.; Armbrust, K. W.; Ellis, J. M.; Hamann, L. G.; Horn, E. J.; Oberg, K. M.; Scholes, G. D.; Hyster, T. K. Quaternary Charge-Transfer Complex Enables Photoenzymatic Intermolecular Hydroalkylation of Olefins. *J. Am. Chem. Soc.* **2021**, *143* (1), 97−102.

(8) Sandoval, B. A.; Meichan, A. J.; Hyster, T. K. Enantioselective Hydrogen Atom Transfer: Discovery of Catalytic Promiscuity in Flavin-Dependent'Ene'-Reductases. *J. Am. Chem. Soc.* **2017**, *139* (33), 11313−11316.

(9) Biegasiewicz, K. F.; Cooper, S. J.; Gao, X.; Oblinsky, D. G.; Kim, J. H.; Garfinkle, S. E.; Joyce, L. A.; Sandoval, B. A.; Scholes, G. D.; Hyster, T. K. Photoexcitation of Flavoenzymes Enables a Stereoselective Radical Cyclization. *Science* **2019**, *364* (6446), 1166−1169.

(10) Fu, H.; Cao, J.; Qiao, T.; Qi, Y.; Charnock, S. J.; Garfinkle, S.; Hyster, T. K. An Asymmetric Sp 3−Sp 3 Cross-Electrophile Coupling Using 'Ene'-Reductases. *Nature* **2022**, *610* (7931), 302−307.

(11) Huang, X.; Wang, B.; Wang, Y.; Jiang, G.; Feng, J.; Zhao, H. Photoenzymatic Enantioselective Intermolecular Radical Hydroalkylation. *Nature* **2020**, *584* (7819), 69−74.

(12) Fu, H.; Hyster, T. K. From Ground-State to Excited-State Activation Modes: Flavin-Dependent "Ene"-Reductases Catalyzed Non-Natural Radical Reactions. *Acc. Chem. Res.* **2024**, *57* (9), 1446−1457.
(13) Björn, L. O. Photoenzymes and Related Topics: An Update. *Photochem. Photobiol.* **2018**, *94* (3), 459−465.
(14) Taylor, A.; Heyes, D. J.; Scrutton, N. S. Catalysis by Nature's Photoenzymes. *Curr. Opin. Struct. Biol.* **2022**, *77*, No. 102491.
(15) Emmanuel, M. A.; Bender, S. G.; Bilodeau, C.; Carceller, J. M.; DeHovitz, J. S.; Fu, H.; Liu, Y.; Nicholls, B. T.; Ouyang, Y.; Page, C. G.; Qiao, T.; Raps, F. C.; Sorigué, D. R.; Sun, S. Z.; Turek-Herman, J.; Ye, Y.; Rivas-Souchet, A.; Cao, J.; Hyster, T. K. Photobiocatalytic Strategies for Organic Synthesis. *Chem. Rev.* **2023**, *123* (9), 5459−5520.
(16) Sorigué, D.; Légeret, B.; Cuiné, S.; Blangy, S.; Moulin, S.; Billon, E.; Richaud, P.; Brugière, S.; Couté, Y.; Nurizzo, D.; Müller, P.; Brettel, K.; Pignol, D.; Arnoux, P.; Li-Beisson, Y.; Peltier, G.; Beisson, F. An Algal Photoenzyme Converts Fatty Acids to Hydrocarbons. *Science* **2017**, *357*, 903−907.
(17) Sorigué, D.; Hadjidemetriou, K.; Blangy, S.; Gotthard, G.; Bonvalet, A.; Coquelle, N.; Samire, P.; Aleksandrov, A.; Antonucci, L.; Benachir, A.; Boutet, S.; Byrdin, M.; Cammarata, M.; Carbajo, S.; Cuiné, S.; Doak, R. B.; Foucar, L.; Gorel, A.; Grünbein, M.; Hartmann, E.; Hienerwadel, R.; Hilpert, M.; Kloos, M.; Lane, T. J.; Légeret, B.; Legrand, P.; Li-Beisson, Y.; Moulin, S. L. Y.; Nurizzo, D.; Peltier, G.; Schirò, G.; Shoeman, R. L.; Sliwa, M.; Solinas, X.; Zhuang, B.; Barends, T. R. M.; Colletier, J. P.; Joffre, M.; Royant, A.; Berthomieu, C.; Weik, M.; Domratcheva, T.; Brettel, K.; Vos, M. H.; Schlichting, I.; Arnoux, P.; Müller, P.; Beisson, F. Mechanism and Dynamics of Fatty Acid Photodecarboxylase. *Science* **2021**, *372*, No. eabd5687.
(18) Hedison, T. M.; Heyes, D. J.; Scrutton, N. S. Making Molecules with Photodecarboxylases: A Great Start or a False Dawn? *Curr. Res. Chem. Biol.* **2022**, *2*, No. 100017.
(19) Guo, X.; Xia, A.; Zhang, W.; Huang, Y.; Zhu, X.; Zhu, X.; Liao, Q. Photoenzymatic Decarboxylation: A Promising Way to Produce Sustainable Aviation Fuels and Fine Chemicals. *Bioresour. Technol.* **2023**, *367*, No. 128232.
(20) Ng, W. Z.; Chan, E. S.; Gourich, W.; Ooi, C. W.; Tey, B. T.; Song, C. P. Perspective on Enzymatic Production of Renewable Hydrocarbon Fuel Using Algal Fatty Acid Photodecarboxylase from Chlorella Variabilis NC64A: Potentials and Limitations. *Renewable Sustainable Energy Rev.* **2023**, *184*, No. 113548.
(21) Sui, Y.; Guo, X.; Zhou, R.; Fu, Z.; Chai, Y.; Xia, A.; Zhao, W. Photoenzymatic Decarboxylation to Produce Hydrocarbon Fuels: A Critical Review. *Mol. Biotechnol.* **2023**, DOI: 10.1007/s12033-023-00775-2.
(22) Huijbers, M. M. E.; Zhang, W.; Tonin, F.; Hollmann, F. Light-Driven Enzymatic Decarboxylation of Fatty Acids. *Angew. Chem., Int. Ed.* **2018**, *57* (41), 13648−13651.
(23) Cha, H. J.; Hwang, S. Y.; Lee, D. S.; Kumar, A. R.; Kwon, Y. U.; Voß, M.; Schuiten, E.; Bornscheuer, U. T.; Hollmann, F.; Oh, D. K.; Park, J. B. Whole-Cell Photoenzymatic Cascades to Synthesize Long-Chain Aliphatic Amines and Esters from Renewable Fatty Acids. *Angew. Chem., Int. Ed.* **2020**, *59* (18), 7024−7028.
(24) Samire, P. P.; Zhuang, B.; Légeret, B.; Baca-Porcel, Á.; Peltier, G.; Sorigué, D.; Aleksandrov, A.; Beisson, F.; Müller, P. Autocatalytic Effect Boosts the Production of Medium-Chain Hydrocarbons by Fatty Acid Photodecarboxylase. *Sci. Adv.* **2023**, *9* (13), No. eadg3881.
(25) Bruder, S.; Moldenhauer, E. J.; Lemke, R. D.; Ledesma-Amaro, R.; Kabisch, J. Drop-in Biofuel Production Using Fatty Acid Photodecarboxylase from Chlorella Variabilis in the Oleaginous Yeast Yarrowia Lipolytica. *Biotechnol. Biofuels* **2019**, *12* (1), 202.
(26) Li, J.; Ma, Y.; Liu, N.; Eser, B. E.; Guo, Z.; Jensen, P. R.; Stephanopoulos, G. Synthesis of High-Titer Alka(e)Nes in Yarrowia Lipolytica Is Enabled by a Discovered Mechanism. *Nat. Commun.* **2020**, *11* (1), No. 6198.
(27) Zhang, W.; Ma, M.; Huijbers, M. M. E.; Filonenko, G. A.; Pidko, E. A.; Van Schie, M.; De Boer, S.; Burek, B. O.; Bloh, J. Z.; Van Berkel, W. J. H.; Smith, W. A.; Hollmann, F. Hydrocarbon Synthesis via Photoenzymatic Decarboxylation of Carboxylic Acids. *J. Am. Chem. Soc.* **2019**, *141* (7), 3116−3120.
(28) Santner, P.; Szabó, L. K.; Chanquia, S. N.; Merrild, A. H.; Hollmann, F.; Kara, S.; Eser, B. E. Optimization and Engineering of Fatty Acid Photodecarboxylase for Substrate Specificity. *ChemCatChem* **2021**, *13* (18), 4038−4046.
(29) Amer, M.; Wojcik, E. Z.; Sun, C.; Hoeven, R.; Hughes, J. M. X.; Faulkner, M.; Yunus, I. S.; Tait, S.; Johannissen, L. O.; Hardman, S. J. O.; Heyes, D. J.; Chen, G. Q.; Smith, M. H.; Jones, P. R.; Toogood, H. S.; Scrutton, N. S. Low Carbon Strategies for Sustainable Bio-Alkane Gas Production and Renewable Energy. *Energy Environ. Sci.* **2020**, *13* (6), 1818−1831.
(30) Ju, S.; Li, D.; Mai, B. K.; Liu, X.; Vallota-Eastman, A.; Wu, J.; Valentine, D. L.; Liu, P.; Yang, Y. Stereodivergent Photobiocatalytic Radical Cyclization through the Repurposing and Directed Evolution of Fatty Acid Photodecarboxylases. *Nat. Chem.* **2024**, *16* (8), 1339−1347.
(31) Gao, J. Hybrid Quantum and Molecular Mechanical Simulations: An Alternative Avenue to Solvent Effects in Organic Chemistry. *Acc. Chem. Res.* **1996**, *29* (6), 298−305.
(32) Senn, H. M.; Thiel, W. QM/MM Methods for Biomolecular Systems. *Angew. Chem., Int. Ed.* **2009**, *48* (7), 1198−1229.
(33) Van Der Kamp, M. W.; Mulholland, A. J. Combined Quantum Mechanics/Molecular Mechanics (QM/MM) Methods in Computational Enzymology. *Biochemistry* **2013**, *52* (16), 2708−2728.
(34) Lipparini, F.; Mennucci, B. Hybrid QM/Classical Models: Methodological Advances and New Applications. *Chem. Phys. Rev.* **2021**, *2* (4), 041303.
(35) Aleksandrov, A.; Bonvalet, A.; Müller, P.; Sorigué, D.; Beisson, F.; Antonucci, L.; Solinas, X.; Joffre, M.; Vos, M. H. Catalytic Mechanism of Fatty Acid Photodecarboxylase: On the Detection and Stability of the Initial Carbonyloxy Radical Intermediate. *Angew. Chem., Int. Ed.* **2024**, *63* (19), No. e202401376.
(36) Goings, J. J.; Hammes-Schiffer, S. Early Photocycle of Slr1694 Blue-Light Using Flavin Photoreceptor Unraveled through Adiabatic Excited-State Quantum Mechanical/Molecular Mechanical Dynamics. *J. Am. Chem. Soc.* **2019**, *141* (51), 20470−20479.
(37) Cupellini, L.; Calvani, D.; Jacquemin, D.; Mennucci, B. Charge Transfer from the Carotenoid Can Quench Chlorophyll Excitation in Antenna Complexes of Plants. *Nat. Commun.* **2020**, *11* (1), No. 662.
(38) Zhu, X.; Thompson, K. C.; Martínez, T. J. Geodesic Interpolation for Reaction Pathways. *J. Chem. Phys.* **2019**, *150* (16), No. 164103.
(39) Kabir, M. P.; Ghosh, P.; Gozem, S. Electronic Structure Methods for Simulating Flavin's Spectroscopy and Photophysics: Comparison of Multi-Reference, TD-DFT, and Single-Reference Wave Function Methods. *J. Phys. Chem. B* **2024**, *128* (31), 7545−7557.
(40) Marcus, R. A. On the Theory of Oxidation-Reduction Reactions Involving Electron Transfer. I. *J. Chem. Phys.* **1956**, *24* (5), 966−978.
(41) Marcus, R. A. Electrostatic Free Energy and Other Properties of States Having Nonequilibrium Polarization. I. *J. Chem. Phys.* **1956**, *24* (5), 979−989.
(42) Pedraza-González, L.; Cignoni, E.; D'Ascenzi, J.; Cupellini, L.; Mennucci, B. How the PH Controls Photoprotection in the Light-Harvesting Complex of Mosses. *J. Am. Chem. Soc.* **2023**, *145* (13), 7482−7494.
(43) Cignoni, E.; Lapillo, M.; Cupellini, L.; Acosta-Gutiérrez, S.; Gervasio, F. L.; Mennucci, B. A Different Perspective for Non-photochemical Quenching in Plant Antenna Complexes. *Nat. Commun.* **2021**, *12* (1), No. 7152.
(44) Blumberger, J. Recent Advances in the Theory and Molecular Simulation of Biological Electron Transfer Reactions. *Chem. Rev.* **2015**, *115* (20), 11191−11238.
(45) Kar, R. K.; Miller, A. F.; Mroginski, M. A. Understanding Flavin Electronic Structure and Spectra. *Wiley Interdiscip. Rev. Comput. Mol. Sci.* **2022**, *12* (2), No. e1541.

(46) Kabir, M. P.; Orozco-Gonzalez, Y.; Gozem, S. Electronic Spectra of Flavin in Different Redox and Protonation States: A Computational Perspective on the Effect of the Electrostatic Environment. *Phys. Chem. Chem. Phys.* **2019**, *21* (30), 16526−16537.
(47) Nottoli, M.; Mazzeo, P.; Lipparini, F.; Cupellini, L.; Mennucci, B. A ΔSCF Model for Excited States within a Polarisable Embedding. *Mol. Phys.* **2023**, *121* (9−10), No. 2089605.
(48) Mazzeo, P.; Hashem, S.; Lipparini, F.; Cupellini, L.; Mennucci, B. Fast Method for Excited-State Dynamics in Complex Systems and Its Application to the Photoactivation of a Blue Light Using Flavin Photoreceptor. *J. Phys. Chem. Lett.* **2023**, *14* (5), 1222−1229.
(49) Heyes, D. J.; Lakavath, B.; Hardman, S. J. O.; Sakuma, M.; Hedison, T. M.; Scrutton, N. S. Photochemical Mechanism of Light-Driven Fatty Acid Photodecarboxylase. *ACS Catal.* **2020**, *10* (12), 6691−6696.
(50) Wu, R.; Li, X.; Wang, L.; Zhong, D. Ultrafast Dynamics and Catalytic Mechanism of Fatty Acid Photodecarboxylase. *Angew. Chem., Int. Ed.* **2022**, *61* (50), No. e202209180.
(51) Šali, A.; Blundell, T. L. Comparative Protein Modelling by Satisfaction of Spatial Restraints. *J. Mol. Biol.* **1993**, *234* (3), 779−815.
(52) Georgescu, R. E.; Alexov, E. G.; Gunner, M. R. Combining Conformational Flexibility and Continuum Electrostatics for Calculating PKas in Proteins. *Biophys. J.* **2002**, *83* (4), 1731−1748.
(53) Song, Y.; Mao, J.; Gunner, M. R. MCCE2: Improving Protein PKa Calculations with Extensive Side Chain Rotamer Sampling. *J. Comput. Chem.* **2009**, *30* (14), 2231−2247.
(54) Case, D. A.; Aktulga, H. M.; Belfon, K.; Ben-Shalom, I. Y.; Berryman, J. T.; Brozell, S. R.; Cerutti, D. S.; Cheatham, T. E., III; Cisneros, G. A.; Cruzeiro, V. W. D.; Darden, T. A.; Duke, R. E.; Giambasu, G.; Gilson, M. K.; Gohlke, H.; Goetz, A. W.; Harris, R.; Izadi, A.; Izmailov, S. A.; Kasavajhala, K.; Kaymak, M. C.; King, E.; Kovalenko, A.; Kurtzman, T.; Lee, T. S.; LeGrand, S.; Li, P.; Lin, C.; Liu, J.; Luchko, T.; Luo, R.; Machado, M.; Man, V.; Manathunga, M.; Merz, K. M.; Miao, Y.; Mikhailovskii, O.; Monard, G.; Nguyen, H.; O'Hearn, K. A.; Onufriev, A.; Pan, F.; Pantano, S.; Qi, R.; Rahnamoun, A.; Roe, D. R.; Roitberg, A.; Sagui, C.; Schott-Verdugo, S.; Shajan, A.; Shen, J.; Simmerling, C. L.; Skrynnikov, N. R.; Smith, J.; Swails, J.; Walker, R. C.; Wang, J.; Wang, J.; Wei, H.; Wolf, R. M.; Wu, X.; Xiong, Y.; Xue, Y.; York, D. M.; Zhao, S.; Kollman, P. A. *Amber 2022*; University of California: San Francisco, 2022.
(55) Maier, J. A.; Martinez, C.; Kasavajhala, K.; Wickstrom, L.; Hauser, K. E.; Simmerling, C. Ff14SB: Improving the Accuracy of Protein Side Chain and Backbone Parameters from Ff99SB. *J. Chem. Theory Comput.* **2015**, *11* (8), 3696−3713.
(56) Jorgensen, W. L.; Chandrasekhar, J.; Madura, J. D.; Impey, R. W.; Klein, M. L. Comparison of Simple Potential Functions for Simulating Liquid Water. *J. Chem. Phys.* **1983**, *79* (2), 926−935.
(57) Wang, J.; Wolf, R. M.; Caldwell, J. W.; Kollman, P. A.; Case, D. A. Development and Testing of a General Amber Force Field. *J. Comput. Chem.* **2004**, *25* (9), 1157−1174.
(58) Schneider, C.; Sühnel, J. A Molecular Dynamics Simulation of the Flavin Mononucleotide−RNA Aptamer Complex. *Biopolymers* **1999**, *50* (3), 287−302.
(59) Meagher, K. L.; Redman, L. T.; Carlson, H. A. Development of Polyphosphate Parameters for Use with the AMBER Force Field. *J. Comput. Chem.* **2003**, *24* (9), 1016−1025.
(60) Tomasi, J.; Mennucci, B.; Cammi, R. Quantum Mechanical Continuum Solvation Models. *Chem. Rev.* **2005**, *105* (8), 2999−3094.
(61) Chung, L. W.; Sameera, W. M. C.; Ramozzi, R.; Page, A. J.; Hatanaka, M.; Petrova, G. P.; Harris, T. V.; Li, X.; Ke, Z.; Liu, F.; Li, H.-B.; Ding, L.; Morokuma, K. The ONIOM Method and Its Applications. *Chem. Rev.* **2015**, *115* (12), 5678−5796.
(62) Frisch, M. J.; Trucks, G. W.; Schlegel, H. B.; Scuseria, G. E.; Robb, M. A.; Cheeseman, J. R.; Scalmani, G.; Barone, V.; Petersson, G. A.; Nakatsuji, H.; Li, X.; Caricato, M.; Marenich, A. V.; Bloino, J.; Janesko, B. G.; Gomperts, R.; Mennucci, B.; Hratchian, H. P.; Ortiz, J. V.; Izmaylov, A. F.; Sonnenberg, J. L.; Williams-Young, D.; Ding, F.; Lipparini, F.; Egidi, F.; Goings, J.; Peng, B.; Petrone, A.; Henderson, T.; Ranasinghe, D.; Zakrzewski, V. G.; Gao, J.; Rega, N.; Zheng, G.; Liang, W.; Hada, M.; Ehara, M.; Toyota, K.; Fukuda, R.; Hasegawa, J.; Ishida, M.; Nakajima, T.; Honda, Y.; Kitao, O.; Nakai, H.; Vreven, T.; Throssell, K.; Montgomery, J. A. J.; Peralta, J. E.; Ogliaro, F.; Bearpark, M. J.; Heyd, J. J.; Brothers, E. N.; Kudin, K. N.; Staroverov, V. N.; Keith, T. A.; Kobayashi, R.; Normand, J.; Raghavachari, K.; Rendell, A. P.; Burant, J. C.; Iyengar, S. S.; Tomasi, J.; Cossi, M.; Millam, J. M.; Klene, M.; Adamo, C.; Cammi, R.; Ochterski, J. W.; Martin, R. L.; Morokuma, K.; Farkas, O.; Foresman, J. B.; Fox, D. J. *Gaussian 16*, Revision A.03; Gaussian, Inc.: Wallingford, CT, 2016.
(63) Hirata, S.; Head-Gordon, M. Time-Dependent Density Functional Theory within the Tamm−Dancoff Approximation. *Chem. Phys. Lett.* **1999**, *314* (3), 291−299.
(64) Bondanza, M.; Nottoli, M.; Cupellini, L.; Lipparini, F.; Mennucci, B. Polarizable Embedding QM/MM: The Future Gold Standard for Complex (Bio)Systems? *Phys. Chem. Chem. Phys.* **2020**, *22* (26), 14433−14448.
(65) Nottoli, M.; Bondanza, M.; Mazzeo, P.; Cupellini, L.; Curutchet, C.; Loco, D.; Lagardère, L.; Piquemal, J.-P.; Mennucci, B.; Lipparini, F. QM/AMOEBA Description of Properties and Dynamics of Embedded Molecules. *WIREs Comput. Mol. Sci.* **2023**, *13* (6), No. e1674.
(66) Ponder, J. W.; Wu, C.; Ren, P.; Pande, V. S.; Chodera, J. D.; Schnieders, M. J.; Haque, I.; Mobley, D. L.; Lambrecht, D. S.; DiStasio, R. A. J.; Head-Gordon, M.; Clark, G. N. I.; Johnson, M. E.; Head-Gordon, T. Current Status of the AMOEBA Polarizable Force Field. *J. Phys. Chem. B* **2010**, *114* (8), 2549−2564.
(67) Ren, P.; Wu, C.; Ponder, J. W. Polarizable Atomic Multipole-Based Molecular Mechanics for Organic Molecules. *J. Chem. Theory Comput.* **2011**, *7* (10), 3143−3161.
(68) Hsu, C.-P.; You, Z.-Q.; Chen, H.-C. Characterization of the Short-Range Couplings in Excitation Energy Transfer. *J. Phys. Chem. C* **2008**, *112* (4), 1204−1212.
(69) Yang, C.-H.; Hsu, C.-P. A Multi-State Fragment Charge Difference Approach for Diabatic States in Electron Transfer: Extension and Automation. *J. Chem. Phys.* **2013**, *139* (15), No. 154104.
(70) Nottoli, M.; Jurinovich, S.; Cupellini, L.; Gardiner, A. T.; Cogdell, R.; Mennucci, B. The Role of Charge-Transfer States in the Spectral Tuning of Antenna Complexes of Purple Bacteria. *Photosynth. Res.* **2018**, *137* (2), 215−226.
(71) Bussi, G.; Donadio, D.; Parrinello, M. Canonical Sampling through Velocity Rescaling. *J. Chem. Phys.* **2007**, *126* (1), 014101.
(72) Hashem, S.; Macaluso, V.; Nottoli, M.; Lipparini, F.; Cupellini, L.; Mennucci, B. From Crystallographic Data to the Solution Structure of Photoreceptors: The Case of the AppA BLUF Domain. *Chem. Sci.* **2021**, *12* (40), 13331−13342.
(73) Macaluso, V.; Hashem, S.; Nottoli, M.; Lipparini, F.; Cupellini, L.; Mennucci, B. Ultrafast Transient Infrared Spectroscopy of Photoreceptors with Polarizable QM/MM Dynamics. *J. Phys. Chem. B* **2021**, *125* (36), 10282−10292.
(74) Lagardère, L.; Jolly, L.-H.; Lipparini, F.; Aviat, F.; Stamm, B.; Jing, Z. F.; Harger, M.; Torabifard, H.; Cisneros, G. A.; Schnieders, M. J.; Gresh, N.; Maday, Y.; Ren, P. Y.; Ponder, J. W.; Piquemal, J.-P. Tinker-HP: A Massively Parallel Molecular Dynamics Package for Multiscale Simulations of Large Complex Systems with Advanced Point Dipole Polarizable Force Fields. *Chem. Sci.* **2018**, *9* (4), 956−972.
(75) Frisch, M. J.; Trucks, G. W.; Schlegel, H. B.; Scuseria, G. E.; Robb, M. A.; Cheeseman, J. R.; Scalmani, G.; Barone, V.; Petersson, G. A.; Nakatsuji, H.; Li, X.; Caricato, M.; Marenich, A. V.; Bloino, J.; Janesko, B. G.; Gomperts, R.; Mennucci, B.; Hratchian, H. P.; Ortiz, J. V.; Izmaylov, A. F.; Sonnenberg, J. L.; Williams-Young, D.; Ding, F.; Lipparini, F.; Egidi, F.; Goings, J.; Peng, B.; Petrone, A.; Henderson, T.; Ranasinghe, D.; Zakrzewski, V. G.; Gao, J.; Rega, N.; Zheng, G.; Liang, W.; Hada, M.; Ehara, M.; Toyota, K.; Fukuda, R.; Hasegawa, J.; Ishida, M.; Nakajima, T.; Honda, Y.; Kitao, O.; Nakai, H.; Vreven, T.; Throssell, K.; Montgomery, J. A. J.; Peralta, J. E.; Ogliaro, F.; Bearpark, M. J.; Heyd, J. J.; Brothers, E. N.; Kudin, K. N.; Staroverov,

https://doi.org/10.1021/jacsau.4c00853
JACS Au 2025, 5, 158−168

V. N.; Keith, T. A.; Kobayashi, R.; Normand, J.; Raghavachari, K.; Rendell, A. P.; Burant, J. C.; Iyengar, S. S.; Tomasi, J.; Cossi, M.; Millam, J. M.; Klene, M.; Adamo, C.; Cammi, R.; Ochterski, J. W.; Martin, R. L.; Morokuma, K.; Farkas, O.; Foresman, J. B.; Fox, D. J. *Gaussian Development Version*, Revision J.19; Gaussian, Inc.: Wallingford, CT, 2020.

https://doi.org/10.1021/jacsau.4c00853
JACS Au 2025, 5, 158−168